In-situ confocal microscopy study on dissolution kinetics of calcium aluminate inclusions in $CaO–Al_2O_3–SiO_2$ type steelmaking slags

Wang, Guang; Nabeel, Muhammad; Mu, Wangzhong; Phillion, A. B.; Dogan, Neslihan

DOI
10.1007/s42243-024-01397-x

Publication date
2025

Document Version
Final published version

Published in
Journal of Iron and Steel Research International

J. Iron Steel Res. Int.
https://doi.org/10.1007/s42243-024-01397-x

ORIGINAL PAPER

In-situ confocal microscopy study on dissolution kinetics of calcium aluminate inclusions in $CaO–Al_2O_3–SiO_2$ type steelmaking slags

Guang Wang[1] · Muhammad Nabeel[1] · Wangzhong Mu[2,3] · A.B. Phillion[1] · Neslihan Dogan[1,4]

Received: 30 July 2024 / Revised: 5 September 2024 / Accepted: 10 September 2024

Abstract
Dissolution kinetics of $CaO·2Al_2O_3$ (CA_2) particles in a synthetic $CaO–Al_2O_3–SiO_2$ steelmaking slag system have been investigated using the high-temperature confocal laser scanning microscope. Effects of temperature (i.e., 1500, 1550, and 1600 °C) and slag composition on the dissolution time of CA2 particles are investigated, along with the time dependency of the projection area of the particle during the dissolution process. It is found that the dissolution rate was enhanced by either an increase in temperature or a decrease in slag viscosity. Moreover, a higher ratio of CaO/Al_2O_3 (C/A) leads to an increased dissolution rate of CA_2 particle at 1600 °C. Thermodynamic calculations suggested the dissolution product, i.e., melilite, formed on the surface of the CA_2 particle during dissolution in slag with a C/A ratio of 3.8 at 1550 °C. Scanning electron microscopy equipped with energy dispersive X-ray spectrometry analysis of as-quenched samples confirmed the dissolution path of CA_2 particles in slags with C/A ratios of 1.8 and 3.8 as well as the melilite formed on the surface of CA_2 particle. The formation of this layer during the dissolution process was identified as a hindrance, impeding the dissolution of CA_2 particle. A valuable reference for designing or/and choosing the composition of top slag for clean steel production is provided, especially using calcium treatment during the secondary refining process.

Keywords In-situ observation · Dissolution kinetics · Confocal laser scanning microscope · Calcium aluminate inclusion · Steelmaking slag · Clean steel

1 Introduction

The presence of non-metallic inclusions (NMIs) in steel degrades the mechanical properties of final product, like tensile strength and corrosion resistance [1, 2]. Moreover, specific types of NMIs can cause some engineering problems, like clogging of the submerged entry nozzle (SEN) during continuous casting [3]. As a result, it is crucial to minimize the presence of NMIs in steels.

Different approaches have been developed and applied to control and remove NMIs during the secondary steelmaking process. Two common approaches are introduced here. The first one is the modification of composition and morphology of NMIs in liquid steel. A well-known example is the calcium treatment for aluminum killed steel, which modifies the solid alumina inclusions to become liquid or semi-liquid calcium aluminates and changes their shape from irregular to spherical. These modifications significantly reduce the risk of SEN clogging and product defects [4–6]. However, inadequate calcium addition can result in incomplete alteration of alumina inclusions, leading to the creation of undesired solid inclusions like $CaO·2Al_2O_3$ (CA_2) and $CaO·6Al_2O_3$ (CA_6). If these compounds form, there is an enhanced risk of blockages within the SEN during continuous casting. The second approach is the removal of NMIs from the liquid steel into the molten

✉ Guang Wang
wangg84@mcmaster.ca

✉ Neslihan Dogan
n.d.dogan@tudelft.nl

[1] Department of Materials Science and Engineering, McMaster University, Hamilton L8S4L7, Ontario, Canada

[2] Department of Materials Science and Engineering, KTH Royal Institute of Technology, Stockholm 10044, Sweden

[3] Engineering Materials, Department of Engineering Science and Mathematics, Luleå University of Technology, Luleå 97187, Sweden

[4] Department of Materials Science and Engineering, Delft University of Technology, Delft 2628CD, The Netherlands

Published online: 21 January 2025

slag. The removal of NMIs out of the liquid steel can occur in the ladle, tundish, or continuous caster. Irrespective of the process, removal occurs in three stages: flotation of the inclusion from bulk steel to the steel–slag interface, separation of the inclusion from the steel–slag interface, and dissolution of the inclusion into the steelmaking slag. For the last stage, a rapid dissolution of NMIs is desirable. If the dissolution kinetics of NMIs are insufficient, they may oscillate at the slag interface, elevating the risk of re-entrainment.

Over the past few decades, different approaches have been applied to investigate the dissolution of NMIs in the steelmaking slags, and especially, temperature is the key parameter to be investigated [7–9]. The most common approach is the so-called rotating finger test, or named rotating cylinder test and rotating dip test. For this method, firstly, an oxide cylinder with a diameter of about 1 cm is inserted into the liquid slag; and secondly, the dissolution kinetics are determined from the reduction in the diameter of the cylinder. While this method has provided much insight into NMI's dissolution, a significant limitation is the substantial difference in size between the immersed oxide cylinder and oxide inclusions that occurs during the process. Potentially, the difference raises doubts regarding the applicability of data obtained from centimeter-sized samples to dissolution kinetics at micron-scale dimensions.

The high-temperature confocal laser scanning microscope (HT-CLSM) is a robust facility that has been developed in the last two decades and provides an in-situ real-time observation capability for investigating the behavior of micron-sized NMIs under conditions relevant to the steelmaking process. Sridhar and Cramb [10] first reported the dissolution process of alumina inclusion in the molten slag. Since then, several studies have been carried out to study the dissolution of different types of inclusions in molten slags. These studies were primarily directed towards the elucidation of the dissolution mechanisms and kinetics of single-phase NMIs including Al_2O_3 [1, 10–21], MgO [1, 13, 15, 22], CaO [23, 24], and SiO_2 [2, 25, 26], as well as the complex NMIs, $MgAl_2O_4$ [1, 13, 15, 27] and Al_2TiO_5 [28–30] in the steelmaking slag systems, e.g., $CaO–Al_2O_3–SiO_2$ with or without MgO at high temperature ranging from 1250 to 1630 °C. Besides the above mentioned inclusion types, limited information is available in the open literature regarding the dissolution kinetics of calcium aluminate inclusions, e.g., CA_2 [6] in steelmaking slags. Miao et al. [6] conducted pioneering research on the dissolution of CA_2 in two $CaO–Al_2O_3–SiO_2$ type slags at different temperatures. Their findings indicated that mass transfer of the dissolving species within the molten slag is the rate-limiting step for CA_2 particles dissolution. Furthermore, they observed that the dissolution rate of CA_2 particles was enhanced by higher temperature and lower SiO_2 content in slag. However, the study employed two types of slags with different CaO/Al_2O_3 (C/A) ratios and SiO_2 contents to study the effect of SiO_2 content on the dissolution rate of CA_2 particles. This introduces uncertainty regarding the role of the C/A ratio in accelerating CA_2 dissolution. Moreover, the impact of one of the most critical factors, the C/A ratio of the refining slag, affecting the total oxygen in molten steel [31], was not explored in relation to the dissolution kinetics of the CA_2 particles. Systematic study of the important process parameters is required for a better understanding of the dissolution kinetics and mechanisms of these complex inclusions for achieving clean steel production during the secondary steelmaking process.

This study fills the above-mentioned knowledge gap by combining in-situ observation of CA_2 particle dissolution via HT-CLSM, thermodynamic calculations, and electron microscopy. The effect of temperature and slag properties (C/A ratio and slag viscosity) was quantified. Moreover, the dissolution path of CA_2 in two slags at 1550 °C was determined.

2 Methodology

2.1 Materials

Steelmaking type slags were synthesized in the laboratory using high purity (> 99.5%) laboratory-grade powders of $CaCO_3$, CaO, SiO_2 and Al_2O_3 obtained from Alfa Aesar, USA. The CaO powder was roasted at 1100 °C for 12 h under air before the use to eliminate moisture and decompose any residual $CaCO_3$ present in the powder.

2.1.1 CA_2 particle preparation

For the preparation of CA_2 particles, a total of 100 g $CaCO_3$ and Al_2O_3 powders in stochiometric proportions, were prepared. The mixture underwent a mixing process to get the well mixed powder. The details of the mixing process can be found elsewhere [6]. The powder was lightly moistened with approximately 5 wt.% distilled water. Approximately 20 g the dried and moistened powder was compacted into a pellet with a diameter of 2.5 cm and a height of 2 cm. A pressure of 20 MPa was applied for 30 s to ensure proper pellet formation. These pellets were then transferred into an alumina crucible and subjected to sintering in a vertical tube furnace. The sintering process involved heating the pellets at a rate of 10 °C/min until reaching 1600 °C followed by an isothermally holding for 24 h. Subsequently, the pellets were gradually furnace cooled at 10 °C/min to room temperature. Throughout the entire sintering process, argon gas was

injected to maintain an inert atmosphere. The sintered pellets were characterized by performing room-temperature powder X-ray diffraction (XRD) measurements using a PANalytical X'Pert diffraction instrument, which uses a copper source with a wavelength of 1.54056 Å. A Rietveld refinement of the XRD pattern was performed using the FULLPROF suite. As can be seen in Fig. 1, the acquired XRD patterns matched those of the standard reference CA_2 [32]. Notably, no additional phases were detected, confirming the successful preparation of high-purity CA_2.

2.1.2 Slag preparation

Several key factors were considered when designing the slag composition for dissolution experiments using HT-CLSM. First, the slag had to be transparent (or semi-transparent) to enable clear observation of particle dissolution. Second, the liquidus temperature of the slag needed to be lower than that of the inclusions to ensure that the slag was completely liquid and had a homogeneous composition. Finally, slags were designed to provide different C/A ratios and different SiO_2 contents. CaO and Al_2O_3 were included to enhance the wettability of the slag with inclusions, while SiO_2 supported the transparency of the slag. Transition-metal oxides such as FeO and CrO_x were avoided as they increased the opacity of the slag.

The preparation of slag samples involved mixing powder of CaO, SiO_2, and Al_2O_3 in stochiometric amounts and heating them to the target temperature, i.e., 50 °C higher than the theoretical liquidus temperature of the slag. This mixture was fully melted in a platinum crucible placed in a box furnace and then held isothermally for 4 h to ensure that homogenization. Post-preparation, the composition of slag was confirmed by inductively coupled plasma optical emission spectroscopy (ICP-OES).

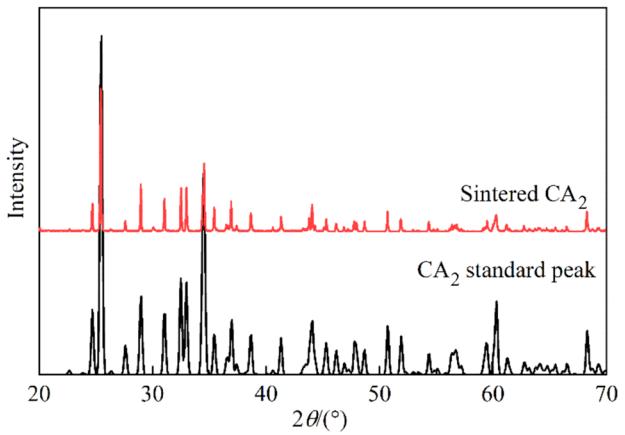

Fig. 1 XRD patterns of CA_2 prepared by sintering at 1600 °C for 24 h. 2θ—Diffraction angle

Five different slags were prepared, with the composition shown in Table 1. Slag C/A_1, C/A_2, and C/A_4 had a similar SiO_2 content but different C/A ratios to study the effect of C/A ratio on CA_2 dissolution kinetics; Slag S50, S40, and S10 had a similar C/A ratio and but different SiO_2 contents. These were fabricated to investigate the effect of slag viscosity on CA_2 dissolution kinetics. The influence of temperature on the dissolution of CA_2 particles was conducted in slag C/A_1. Please note that slag C/A_2 and S40 are identical. The different nomenclatures are used in order to facilitate the discussion of experimental results.

2.2 In-situ observation experiments

An HT-CLSM (VL2000DX-SVF17SP, Yonekura) was employed to perform the dissolution experiments on the CA_2 particles while making continuous in-situ observations. The technical details of the HT-CLSM facility and operation procedure can be found elsewhere [33]. The experiment was conducted as follows. Firstly, approximately 0.15 g slag was pre-melted in a Pt crucible of 5 mm in diameter and 6 mm in height within the high temperature furnace via fast heating and cooling. Secondly, a CA_2 particle was placed on the top of the pre-melted slag. Third, the CA_2–slag assembly was heated to the test temperature following a specified heating profile. Finally, the dissolution process was recorded via HT-CLSM at a frame rate of 10 Hz. To avoid changing the composition of the slag, the mass of the CA_2 particle was kept very small, and less than 0.1% of the pre-melted slag.

Figure 2 illustrates the entire sample assembly. As can be seen, the Pt crucible, slag, and the CA_2 particle were positioned within an alumina crucible, and on the top of a sample holder. A B-type thermocouple, sheathed in an alumina tube, was affixed to the base of the sample holder to measure temperature. This setup resulted in a temperature gradient between the slag surface and the bottom of the alumina crucible; temperature calibration was performed using a pure iron disc of 5 mm in diameter and 2 mm in height. This revealed a temperature difference of around + 17 °C between the surface of the iron disc and the thermocouple. It should be noted that the molten slag wetted the Pt crucible and showed a concave surface; however, this does not affect the observation of the dissolution process.

Each test followed the same thermal profile, as shown in Fig. 3. A rapid heating rate of 1000 °C/min was used to elevate the sample temperature to a value of 50 °C lower than each testing temperature. Subsequently, a lower heating rate of 50 °C/min was used to heat the sample to the testing temperature. This approach served to mitigate the premature dissolution of CA_2 particle without overheating past the desired temperature. To ensure

Table 1 Slag composition and experimental temperatures

Slag	Composition/wt.%			C/A	*T*/°C
	CaO	Al_2O_3	SiO_2		
C/A_1	29	32	39	0.9	1500, 1550, 1600
C/A_2	38	21	41	1.8	1550, 1600
C/A_4	49	13	38	3.8	1550, 1600
S50	33	18	49	1.8	1550
S40	38	21	41	1.8	1550
S10	52	38	10	1.5	1550

T—Temperature

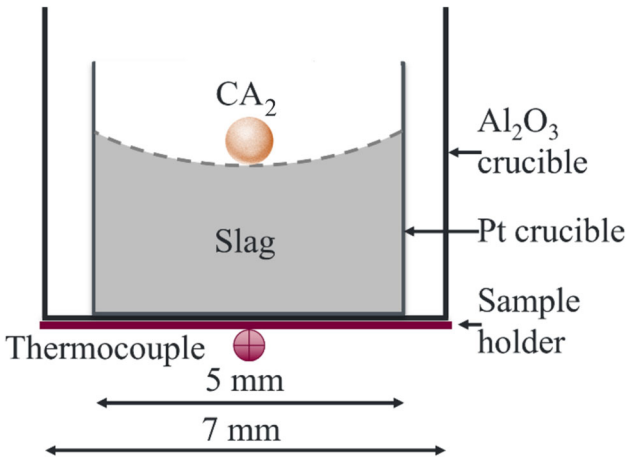

Fig. 2 Sample holder assembly used in high temperature furnace

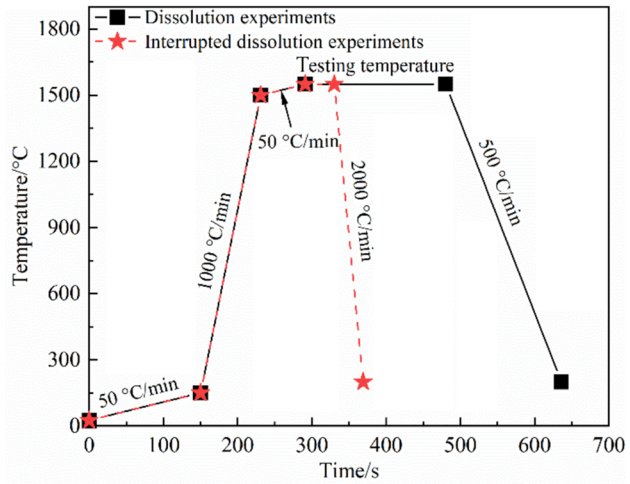

Fig. 3 Thermal cycle for dissolution and interrupted experiments

the experimental repeatability, the dissolution experiments conducted in slag C/A_1 at 1550 °C were repeated 4 times. Note that the onset time of CA_2 dissolution, t_0, was defined as the moment the particle was fully immersed in the molten slag after reaching the testing temperature. Furthermore, the dissolution path of the CA_2 particles in slag C/A_2 and C/A_4 at 1550 °C was interrupted after 90 and 70 s of dissolution by quenching the system using helium with a cooling rate at 2000 °C/min, respectively. After the experiments were completed, scanning electron microscopy-energy dispersive X-ray spectrometry (SEM–EDS) microanalysis was performed on the two quenched samples using a JEOL6610LV. Thermodynamic calculations were carried out using FactSage 8.0 [34]. These calculations included generation of ternary phase diagram, and the determination of slag viscosity using the FToxid databases.

3 Results and discussion

3.1 In-situ observations

In-situ images taken from the CCD camera are used for the evolution of the cross-section area of a CA_2 particle. It is critical that the chosen images focus on the same surface of the CA_2 particle throughout any one dissolution experiment. The area measurements were conducted using the commercial software Image J [35]. To minimize manual error, the measurement of each image measurement was repeated three times, and the average value was calculated. Note that the measurements represent the 2D projection area from the view observable via HT-CLSM.

Figure 4 provides a sequence of images showing the dissolution process of CA_2 in slag C/A_1 at 1500, 1550, and 1600 °C, in slags with different viscosities at 1550 °C, and in slags with different C/A ratios at 1600 °C. Each image within Fig. 4 depicts the CA_2 particle positioned centrally, with the red line denoting the CA_2 particle–slag boundary. The initial area of the CA_2 particle at t_0 is denoted as A_0. Across all three series of experiments, a continuous reduction in area with time is observed, with no discernible product layer evident on the surface of the CA_2 particle. The equivalent radius (r) of CA_2 was calculated

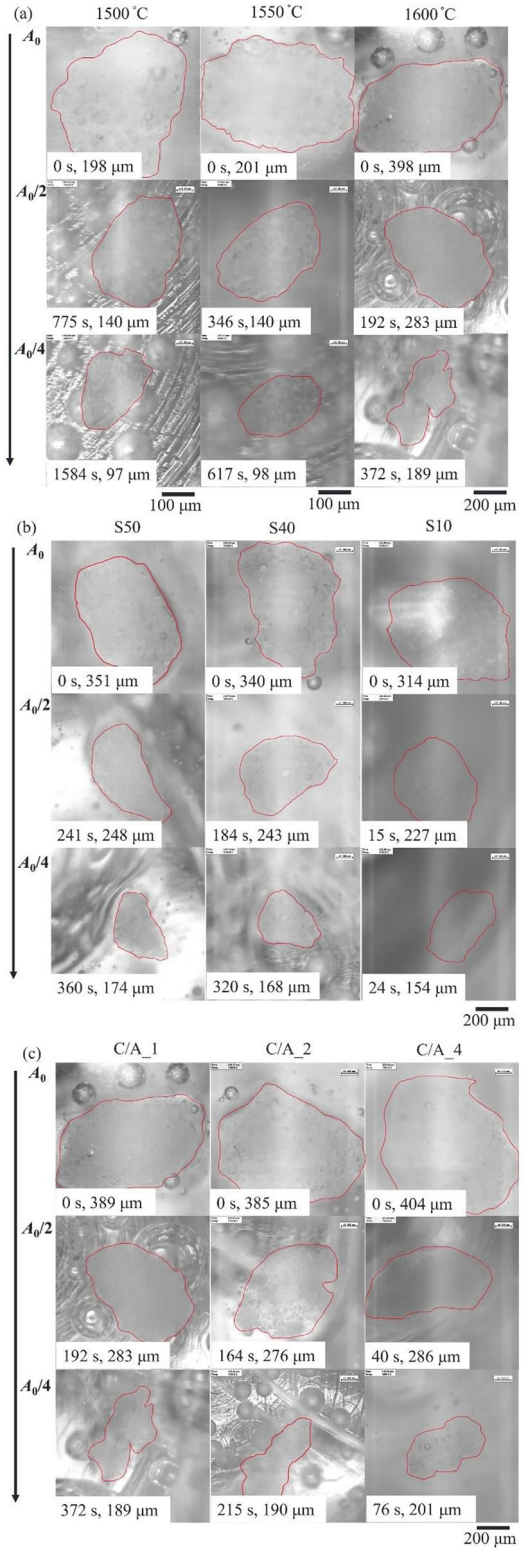

Fig. 4 A sequence of images showing dissolution process of CA_2 particles at different dissolution time of particle and equivalent radii of particle. **a** In slag C/A_1 at 1500, 1550 and 1600 °C; **b** in slag with different viscosities at 1550 °C; **c** in slag with different C/A ratios at 1600 °C

according to the area assuming that CA_2 particle is spherical. As shown in Fig. 4a, the dissolution time at high temperatures is much shorter than that at low temperatures. Further, as shown in Fig. 4b, a decrease in slag viscosity enhances the dissolution time reduction. Note that semi-transparent S10, owing to its low SiO_2 content, results in a less distinct boundary line between CA_2 particles compared to other slags. Finally, as shown in Fig. 4c a higher C/A ratio slag qualitatively correlates with a decreased dissolution time. It is interesting to observe that the CA_2 particle in slag C/A_2 progressively became transparent during dissolution. This phenomenon could potentially be attributed to the faster transport of Ca^{2+} cations compared to AlO_x^{y-} anions in the molten slag [36]. A similar phenomenon was also observed by Liu et al. [22] for the dissolution of a MgO particle in the ternary $CaO–Al_2O_3–SiO_2$ slag at 1600 °C.

In addition to dissolution, the CA_2 particles are observed to rotate, move, and dissociate during experimentation. Figure 5 shows one such process, the dissociation of CA_2 particle in slag C/A_1 at 1550 °C after 846 s of dissolution. At that time, several tiny particles began to detach and move away from the primary particle, as shown in Fig. 5b. Then, all particles continued to dissolve in the molten slag, with the small particles disappearing first due to their smaller size. Since the dissolution rate of NMIs is proportional to their contact area with the molten slag [37, 38], the dissociation of CA_2 particles would augment the contact area, leading to a higher dissolution rate. To mitigate the influence of dissociation on the dissolution kinetics, data after CA_2 dissociation was excluded from the original dataset in all experiments. This approach enabled to isolate

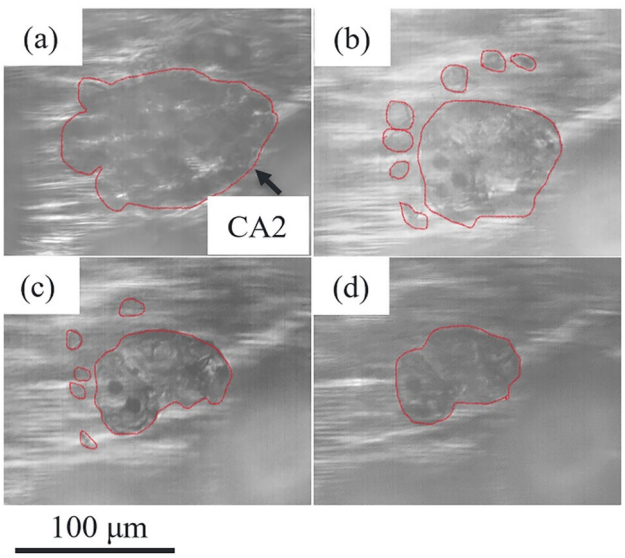

Fig. 5 Dissociation of a particle during dissolution in slag C/A_1 at 1550 °C. **a** 846 s; **b** 876 s; **c** 897 s; **d** 917 s

the effects of dissociation and ensured a more accurate assessment of dissolution kinetics.

3.2 Effect of temperature on dissolution time of CA2 particle

In Fig. 6, the normalized area changes with the time of a CA_2 particle in slag C/A_1 at three distinct temperatures are compared. The dissolution time from A_0 to $A_0/4$ significantly decreased from around 1560 to 617, and to 370 s as the temperature increased from 1500 to 1550 °C, and further to 1600 °C. The influence of temperature on the dissolution time of particles can be elucidated from both thermodynamic and kinetic perspectives [14, 16, 17, 20, 23, 24]. Thermodynamically, assuming local equilibrium at the particle/slag interface, the driving force for particle dissolution is related to the concentration difference (ΔC) of dissolving species between the particle–slag interface and the bulk of the slag. The former can be evaluated from the phase diagram, given by the saturation limit. The temperature significantly impacts the dissolution rate of particles by changing this driving force; generally, an increase in temperature augments the saturation concentration of particle. In the present study, it is assumed that the driving force for CA_2 particle dissolution was the concentration difference between the bulk slag and the saturation content for Al_2O_3 ($\Delta C_{Al_2O_3}$). This assumption is grounded in the fact that the size of the Ca^{2+} cation is smaller than that of the AlO_x^{y-} anion and the diffusion coefficient of Ca^{2+} cation is considerably higher than that of AlO_x^{y-} anion [36]. $\Delta C_{Al_2O_3}$ increased from 458 kg/m^3 (13 wt.%) to 867 kg/m^3 (25 wt.%) with an increase in temperature from 1500 to 1600 °C. Additionally, the activity of the dissolving component at the particle-slag interface and in the bulk slag can influence the dissolution time as well [2]. In this study, the activity of Al_2O_3 at the particle–slag interface is used as the activity of the reactant Al_2O_3 rather than that in the solid CA_2. Using FactSage 8.0 with the FToxid databases [34], the activities of Al_2O_3 in slag C/A_1 at 1500, 1550, and 1600 °C were calculated to be 1.47×10^{-1}, 1.76×10^{-1}, 2.07×10^{-1} at the particle-slag interface, and 7.11×10^{-2}, 7.43×10^{-2}, and 7.74×10^{-2} in the bulk slag, respectively. These results indicate that the difference in Al_2O_3 activity between the particle–slag interface and bulk slag increases as the temperature rises. The increase in this difference results in improved mobility of the AlO_x^{y-} anion within the molten slag, thereby reducing the overall dissolution time.

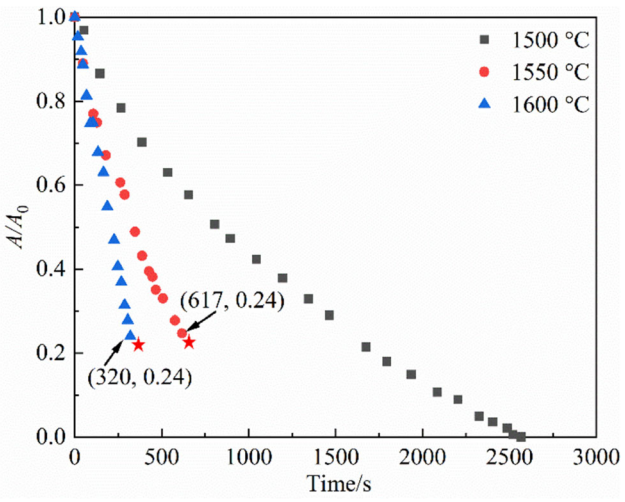

Fig. 6 Evolution in normalized area of a CA_2 particle with time in slag C/A_1 as a function of temperature. Star symbol—Moment when particle dissociation happened, and data after that point are not collected

From the kinetic perspective, temperature changes will also strongly affect the rate of chemical reaction and/or boundary layer diffusion. For a first-order chemical reaction, the rate of particle dissolution is given by:

$$J = k \times C_1 \tag{1}$$

where J is the molar flux of particle per unit area; k is a rate constant; and C_1 is the concentration difference of the dissolving species between solid oxide and bulk slag. For boundary layer diffusion, Fick's first law can be applied to the diffusion across the boundary layer. In this case, the rate of particle dissolution is given by:

$$J = -D \times \frac{C_2}{\delta} \tag{2}$$

where D is the diffusion coefficient of dissolving species; and C_2 is the concentration difference of the dissolving specie between the inside and outside of the boundary layer with thickness δ. An Arrhenius relation describes the temperature dependency of both k and D [14]:

$$k = k_0 \times e^{-E_{a1}/(RT)} \tag{3}$$

$$D = D_0 \times e^{-E_{a2}/(RT)} \tag{4}$$

where k_0 and D_0 are constants; E_{a1} and E_{a2} are activation energies; R is the universal gas constant; and T is the absolute temperature. It is clear from Eqs. (3) and (4) that k and D increase with increasing temperature and therefore so does J, increasing the dissolution rate. In addition to the change in driving force, viscosity impacts the dissolution rate as well. By increasing the temperature from 1500 to 1600 °C, the slag viscosity was calculated to decrease from 3.12 to 1.32 Pa s. The elevated $\Delta C_{Al_2O_3}$ and activity difference, and reduced viscosity are conducive to accelerating the transport of AlO_x^{y-} from the CA_2–slag interface to the bulk slag [2, 6, 20].

3.3 Effect of slag viscosity on dissolution time of CA_2 particle

As shown in Fig. 7, the total dissolution time of the CA_2 particle at 1550 °C exhibited a slight decrease from 800 to 650 s as the viscosity of the slag decreased from 1.35 Pa s (S50) to 0.63 Pa s (S40). A further reduction in the slag viscosity to 0.17 Pa s (S10) resulted in a substantial drop in the total dissolution time to 37 s. The change in dissolution time could be a result of two phenomena: the concentration difference of the dissolving species between the particle–slag interface and the bulk of the slag since each of these slags has different compositions, or the underlying slag structure which directly controls the viscosity (along with slag composition and temperature).

Examining the first phenomenon, it can be seen that the decrease in $\Delta C_{Al_2O_3}$ (kg/m^3) from S50 (1481 kg/m^3, 32 wt.%) to S40 (887 kg/m^3, 26 wt.%) is much larger than the decrease from S40 to S10 (801 kg/m^3, 22 wt.%). This trend is opposite to what was observed for the total dissolution time, and thus, the decrease in the total dissolution time is not so much affected by the change of $\Delta C_{Al_2O_3}$. Miao et al. [6] also reported that the total dissolution time for CA_2 particle in CaO–Al_2O_3–SiO_2 slag with 5.5% SiO_2 content was shorter than that with 46.3% SiO_2 content at the same temperature, despite $\Delta C_{Al_2O_3}$ being lower in 5.5% SiO_2 slag.

Examining the second phenomenon requires a short review of slag structure. One approach is to analyze slag structure through polymer-based and structure-based theories [39], where the slag structure is affected by the content of different oxides present in the slag as they strongly affect the degree of polymerization. SiO_2 is an "acid oxide", and forms an intricate three-dimensional network of anion complexes, whereas CaO is a "basic oxide", and disrupts the three-dimensional networks formed from the SiO_2 oxides. Finally, Al_2O_3 is classified as an "amphoteric oxide" which does not have any distinctive nature. The higher content of network formers, SiO_2 in S50 and S40, significantly surpasses that of S10, while the content of network breakers, like CaO, in S50 and S40 is lower than that in S10. As a result, the presence of complex three-dimensional networks in S10 was comparatively reduced, making it easier for species to transport away from the interface in S10 as compared to in S40 and S50. This reduced resistance facilitates faster dissolution of a CA_2 particle in S10. The degree of polymerization can be quantified using the Q parameter, which in the CaO–Al_2O_3–SiO_2 slag system is determined via [36]

$$Q = 4 - \mathrm{NBO}/X_\mathrm{T} \tag{5}$$

$$\mathrm{NBO} = 2(X_\mathrm{CaO} - 2X_{Al_2O_3}) \tag{6}$$

$$X_\mathrm{T} = X_{SiO_2} + 2X_{Al_2O_3} \tag{7}$$

where NBO is the number of non-bridge oxygen atoms; X_T is the number of tetragonally-coordinated atoms; and X_i is the molar ratio of component i in the slag. A higher Q indicates a greater degree of polymerization of the molten slag and consequently, reduced mobility of dissolving species within the slag. The Q value for S10 is 2.7, contrasting with 3.3 for slag S50 and 3.2 for slag S40. This disparity potentially enhances the transport of AlO_x^{y-} anions from the CA_2 particle–slag interface to the bulk slag, thereby significantly accelerating the dissolution process in slag S10 as compared to that in slags S40 and S50. Therefore, similar Q values would result in close dissolution profiles of S50 and S40. Moreover, as discussed in Ref. [40], Q values between 3 and 4 result in a slag structural unit known as "sheet" whereas slag with Q values between 2 and 3 have a structural unit known as "chain". As a result, the significant decrease in total dissolution time from slags S40 to S10 is primarily affected by the change in slag structure. Finally, it should also be noted that the particle in the S10 experiment was observed to rotate much faster than the particles in slags S40 and S50. This could also have affected the dissolution time.

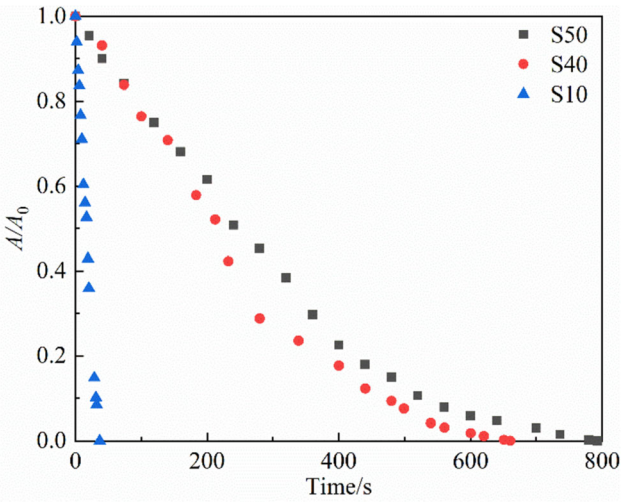

Fig. 7 Evolution in normalized area of a CA_2 particle with time at 1550 °C in slags with different SiO_2 contents and different viscosities

3.4 Effect of C/A ratio on dissolution time of CA_2 particles

The effect of the C/A ratio on the dissolution of CA_2 particles was investigated in three slags having C/A ratios of 0.9, 1.8, and 3.8, each possessing similar SiO_2 content (~ 40%) at 1550 and 1600 °C, respectively. Figure 8a illustrates the normalized area change of CA_2 particles with time at 1600 °C. As can be seen, the dissolution time from A_0 to $A_0/4$ of CA_2 particle at 1600 °C decreased from

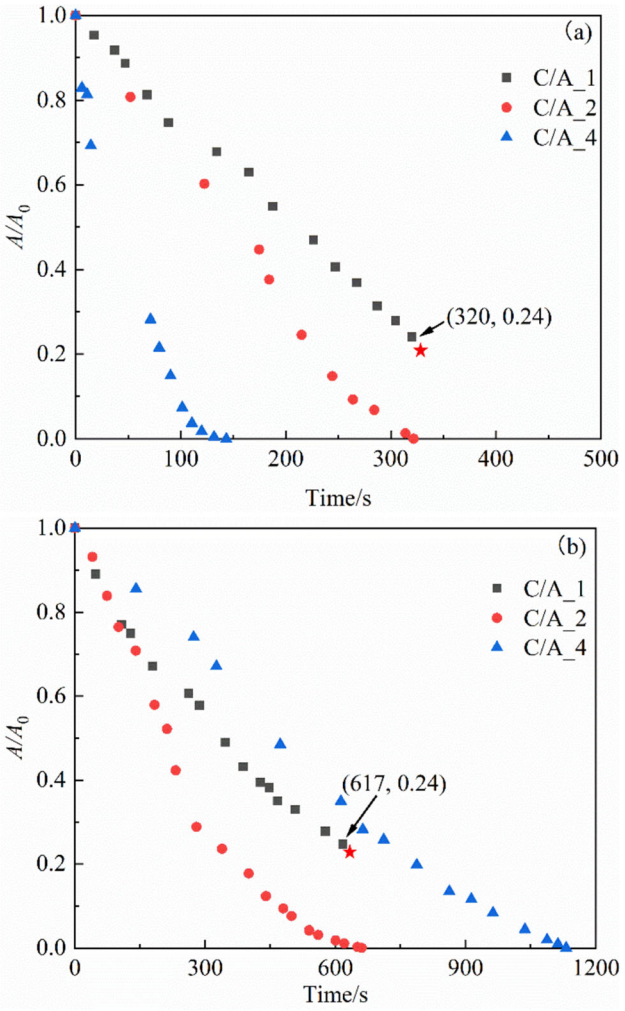

Fig. 8 Evolution of normalized area of a CA_2 particle with time as a function of slag C/A ratio at 1600 (**a**) and 1550 °C (**b**). Star symbol—Moment when particle dissociation happened, and data after that point are not collected

around 315 to 81 s by increasing the C/A ratio from 0.9 to 3.8. This decrease in dissolution time can be attributed to the continuous decrease in slag viscosity from 1.32 to 0.17 Pa s, coupled with an increase in $\Delta C_{Al_2O_3}$ from 867 kg/m^3 (25 wt.%) to 1271 kg/m^3 (40 wt.%) as the C/A ratio increased from 0.9 to 3.8. Both factors, low viscosity, and high driving force, enhanced the dissolution of the CA_2 particle, resulting in a shortened dissolution time. Figure 8b depicts the normalized area change with time in slags with different C/A ratios at 1550 °C. Initially, the dissolution time A_0 to $A_0/4$ of CA_2 particle decreased from 617 to 340 s with an increase in C/A ratio from 0.9 to 1.8. This decrease can be attributed to a reduction in slag viscosity from 2.00 to 0.63 Pa s, coupled with an increase in $\Delta C_{Al_2O_3}$ from 606 kg/m^3 (18 wt.%) to 887 kg/m^3 (49 wt.%). These factors collectively promote the dissolution of the CA_2 particle. However, with a further increase in the C/A ratio to 3.8, the dissolution time unexpectedly increased to 710 s. At this C/A ratio, the viscosity was further decreased to 0.22 Pa s, and $\Delta C_{Al_2O_3}$ dropped to 372 kg/m^3 (26 wt.%). This unexpected behavior suggests that factors beyond $\Delta C_{Al_2O_3}$ and slag viscosity may influence the dissolution kinetics of the CA_2 particle at higher C/A ratios.

To gain increased insight into the effects of the C/A ratio on the dissolution of CA_2 at 1550 °C, the stable phases potentially present in the CA_2, SiO_2–Al_2O_3–CaO system at this temperature were calculated using FactSage 8.0 with FToxid database [34]. Figure 9 shows the relevant ternary diagram, marked with the composition of CA_2, and the initial compositions of slags C/A_1, C/A_2, and C/A_4, as well as black solid lines denoting the two-phase tie lines, dashed lines denoting the expected dissolution paths of CA_2 in the three slags, and the melilite and CA_6 solid phase regions. Although the dissolution is inherently a non-equilibrium process and the dissolution path does not have to be a straight line, the phase diagrams allow for the prediction of phases that may precipitate adjacent to the CA_2 particle.

As can be seen in Fig. 9, at 1550 °C, the composition of all three slags was situated within the fully liquid region. However, the expected dissolution path for slag C/A_1 comes very close to the solid CA_6 phase boundary, while the dissolution path for slag C/A_4 crosses through the solid melilite phase boundary. Thus, the formation of intermediate solid products during the dissolution process, especially for C/A_4, is anticipated. Generally, the formation of an intermediate solid phase on the surface of a solid particle can impede the dissolution of particles by decreasing the transport rate of products from and reactants

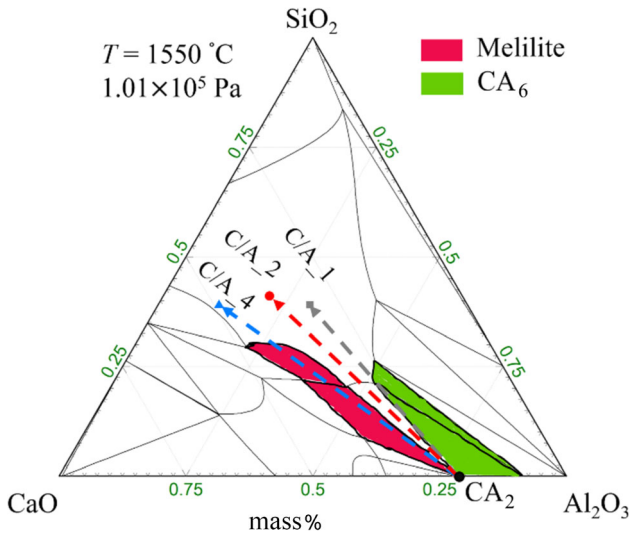

Fig. 9 Prediction of phase stability of CA_2 particle–slag system with FactSage 8.0 at 1550 °C [34]

to the particle surface [23]. In extreme cases, solid products may halt the dissolution if they are densely packed on the particle surface and do not dissolve into the bulk slag. It would show the formation of a solid layer on the surface of the CA_2 particle during its dissolution in slag C/A_4 at 1550 °C, which could have contributed to the observed prolonged dissolution time.

3.5 Determination of dissolution path

To gain deeper insights into the dissolution path of a CA_2 particle in slag C/A_2 and slag C/A_4, SEM–EDS line scan analysis was conducted along the CA_2 particle/slag interface, combined with FactSage thermodynamic calculations. The results are shown in Figs. 10–12. In order to interpret the line scan information with respect to the dissolution path, a mechanism for distinguishing the CA_2 particle, slag C/A_2, slag C/A_4, and melilite must be identified. As shown in Table 2, each of these compounds has a distinct elemental composition. Thus, in the CA_2 particle–slag C/A_2 system, regions at the particle/slag interface that lack Si can be classified as CA_2, while regions where Ca, Al, and Si stably coexist can be labeled as slag C/A_2. Boundary layers are regions having a decreasing Ca and Si compositions while the Al content steadily increases. Similarly, in the CA_2 particle–C/A_4 slag system, the non-Si regions at the particle/slag interface can be designated as CA_2, while regions where Ca, Al, and Si coexist, with Al and Si constituting ~ 20 and ~ 10 wt.%, can be identified as melilite. All other regions can be classified as slag C/A_4.

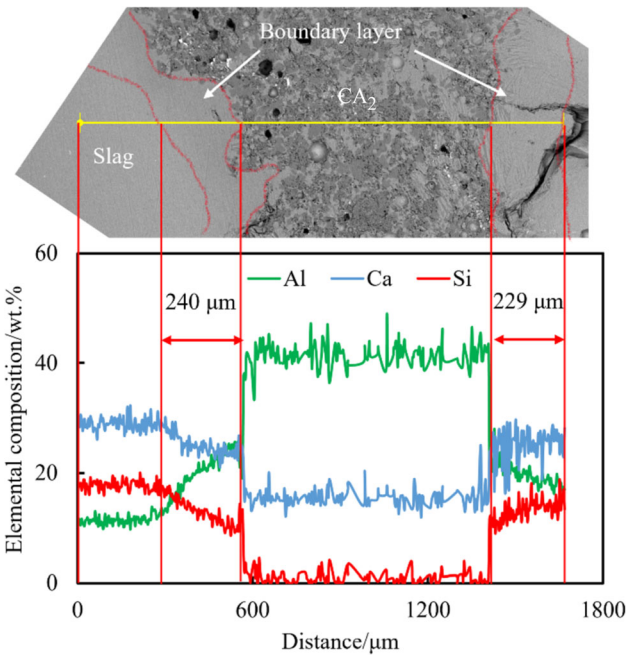

Fig. 10 SEM backscattered electron image and EDS line scan analysis of CA_2 particle–C/A_2 slag interface after 90 s of dissolution at 1550 °C

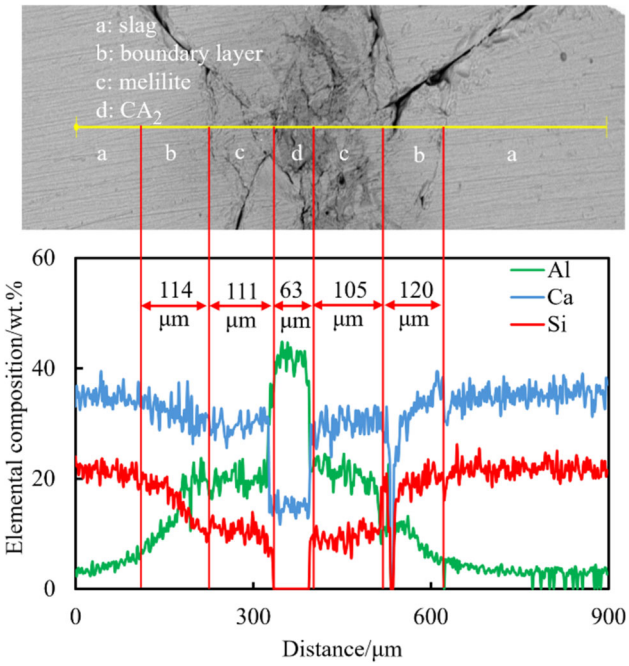

Fig. 11 Back scattered electron image of SEM and EDS line scan analysis of CA_2 particle–C/A_4 slag interface after 70 s of dissolution

Figure 10 displays the backscattered electron image of SEM, and the elements of Ca, Al, and Si distribution obtained from the EDS line scan of the CA_2 particle–C/A_2 slag interface after 90 s of dissolution at 1550 °C. Following the defined criteria, different regions were identified. The dark-colored middle region in the SEM image represents CA_2. An outer layer around the CA_2 particle was determined to be the boundary layer, with a thickness of 230–240 μm. The C/A_2 slag region followed the boundary layer. Moreover, a visible color difference between the slag and the boundary layer was evident in the SEM image. The presence of a boundary layer confirmed that the assumption of the rate determining step for the dissolution process is the mass transfer of AlO_x^{y-} anion in the slag phase. Note that fluctuations in element concentration, especially within the CA_2 particle itself, result from slag penetration into the CA_2 particle through its pores.

Figure 11 shows the back scattered electron image of SEM and the elements Ca, Al, Si distribution by EDS line scan of CA_2 particle–slag C/A_4 interface after 70 s of dissolution at 1550 °C. As can be seen, there is the CA_2 particle in the central region, followed by a layer of melilite 105–111 μm in thickness, and then a boundary layer of about 115 μm.

Figure 12 shows the dissolution paths of CA_2 in slag C/A_2 (circle symbol) and slag C/A_4 (triangle symbol) at

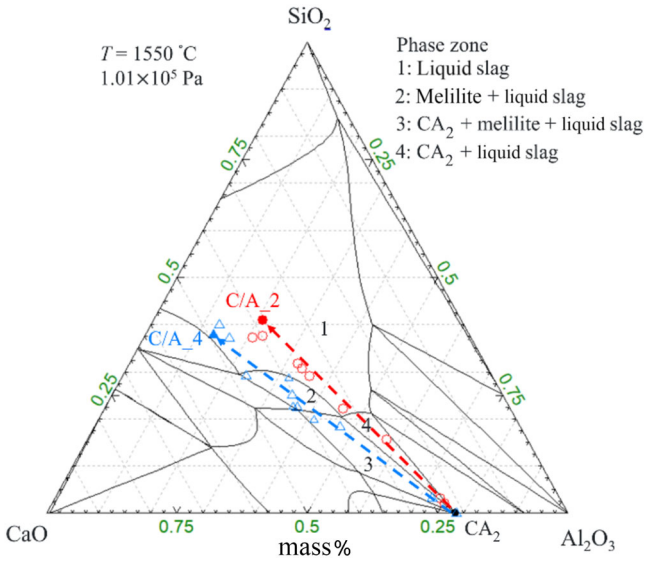

Fig. 12 Dissolution paths of CA_2 in slag C/A_2 and slag C/A_4 at 1550 °C. Circle—EDS line scan results; triangle dash line—thermodynamic calculation results

1550 °C. The data points donated by circle and triangle symbols were taken from the EDS results for both slag systems at different regions along the scanned line. The dashed lines in Fig. 12 donate the theoretical dissolution paths for CA_2 in these two slags. It is evident that the prolonged dissolution of CA_2 in slag C/A_4 compared to slag C/A_2 at 1550 °C is attributed to the formation of the solid melilite phase on the surface of the CA_2 particle. The same reaction product, melilite, for Al_2O_3 dissolution at 1550 °C was also reported by Park et al. [41] in a ternary $53CaO–5Al_2O_3–42SiO_2$ (wt.%) slag and by Sandhage and Yurek [42] in a quaternary $27CaO–21Al_2O_3–42SiO_2–10MgO$ (wt.%) slag, which retarded the dissolution of Al_2O_3.

3.6 Comparison with literature data and practical consideration

The dissolution kinetics between Al_2O_3 and CA_2 particles from the literature and current study were compared since the assumption is that the driving force for CA_2 particle dissolution is the concentration difference between the bulk slag and the saturation content for Al_2O_3 ($\Delta C_{Al_2O_3}$), which is the same as that for Al_2O_3 dissolution. Figure 13 illustrates the average area reduction rate, $\Delta A/\tau$, change as a function of the dissolution factor, $\Delta C_{Al_2O_3}/\mu$. ΔA is area change of particle during the dissolution time, τ, before dissociation happens in comparison with A_0. As can be seen at low $\Delta C_{Al_2O_3}/\mu$ value (< 1000), the difference of $\Delta A/\tau$ between Al_2O_3 and CA_2 particles is small, and it becomes noticeable when $\Delta C_{Al_2O_3}/\mu$ value is higher than 1000. This difference in $\Delta A_0/\tau$ may be due to 1 the greater porosity of lab produced CA_2 particles compared to commercially available dense Al_2O_3 particles; 2) the faster dissolution of CaO in CA_2 particles, which exposes more Al_2O_3 surface to the liquid slag, increasing the contact area between CA_2 particle and molten slag. Moreover, the dissolved CaO from CA_2 particles can act as a network breaker, enhancing the mobility of molten slag.

Table 2 Elemental composition of CA_2 particle, slag C/A_2, slag C/A_4 and melilite at 1550 °C (wt.%)

Composition	Ca	Al	Si
CA_2	15	42	0
C/A_2	27	11	19
C/A_4	34	7	17
Melilite	29	20	10

In the present dissolution experiments, CA_2 particles were only immersed and dissolved into the molten slag under natural convection without any additional forces. In practical applications, the inclusion dissolution typically occurs at the molten steel/top slags interface during the steel refining process, the steel/tundish slags interface, as well as the steel/mold fluxes interface during casting, conditions that more closely resemble natural convection. When the melilite phase forms an out around the CA_2 particle, the CA_2 dissolution rate is slower than that in other cases at the same temperature. The authors believe that the experimental conditions in this study are relevant to the industrial conditions and the findings offer a valuable reference for designing or/and choosing the composition of

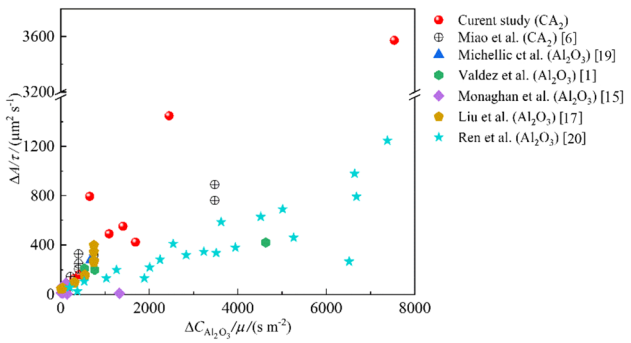

Fig. 13 Average area reduction rate of different types of particles as a function of $\Delta C_{Al_2O_3}/\mu$

top slag, tundish slag, and mold fluxes. This is particularly for Al-killed steel with Ca-treatment, where the calcium is fed into molten steel in the final minutes during the secondary steelmaking, necessitating rapid inclusion dissolution by the top slag.

4 Conclusions

1. The increase in temperature enhances the dissolution rate of CA_2 across all types of $CaO–Al_2O_3–SiO_2$ slags. Furthermore, the dissolution rate of CA_2 significantly decreased when the SiO_2 content increased from 10% to 40%. However, a further increase to 50% SiO_2 did not significantly influence the dissolution rate.
2. The significant decrease in total dissolution time from the slag with 40% SiO_2 to the slag with 10% SiO_2 is primarily affected by the change in slag structure.
3. At 1600 °C, a higher C/A ratio leads to an increased CA_2 dissolution rate. However, it was observed that the formation of melilite layer during the dissolution process acts as a hindrance, impeding the dissolution of the CA_2 particle at 1550 °C.
4. The presence of a boundary layer at the CA_2 particle–C/A_2 slag interface is identified. A solid melilite phase which was observed at the surface of the CA_2 particle in the CA_2 particle–C/A_4 slag system. These observations are consistent with the thermodynamic predictions, validating the accuracy of the experimental and analytical methodologies employed.

Acknowledgements The authors would like to thank the Natural Sciences and Engineering Research Council of Canada (NSERC) for funding this research. This research used a high temperature confocal laser scanning microscope-VL2000DX-SVF17SP funded by Canada Foundation for Innovation John Evans Leaders Fund (CFI JELF, Project Number: 32826), a PANalytical X'Pert diffraction instrument located at the Centre for crystal growth, Brockhouse Institute for Materials Research, and a scanning electron microscope-JEOL 6610 located at the Canadian Centre for Electron Microscopy at McMaster University. W. Mu would like to acknowledge Swedish Iron and Steel Research Office (Jernkonteret), STINT and SSF for supporting the time for international collaboration research regarding clean steel.

Declarations

Conflict of interest Wangzhong Mu is a youth editorial board member for *Journal of Iron and Steel Research International* and was not involved in the editorial review or the decision to publish this article. On behalf of all authors, the corresponding author states that there is no conflict of interest.

References

[1] M. Valdez, K. Prapakorn, A.W. Cramb, S. Seetharaman, Steel Res. 72 (2001) 291–297.
[2] S. Feichtinger, S.K. Michelic, Y.B. Kang, C. Bernhard, J. Am. Ceram. Soc. 97 (2014) 316–325.
[3] S. Waterfall S. Sun, N. Strobl, D. Liao, D. Holdridge, in: J.Y. Hwang, T. Jiang, M.W Kennedy (Eds.), 8th International Symposium on High-Temperature Metallurgical Processing, Springer, San Diego, USA, 2017, pp. 347–57.
[4] W. Yang, L. Zhang, X. Wang, Y. Ren, X. Liu, Q. Shan, ISIJ Int. 53 (2013) 1401–1410.
[5] L. Zhang, Y. Liu, Y. Zhang, W. Yang, W. Chen, Metall. Mater. Trans. B 49 (2018) 1841–1859.
[6] K. Miao, A. Haas, M. Sharma, W. Mu, N. Dogan, Metall. Mater. Trans. B 49 (2018) 1612–1623.
[7] M. Guo, P.T. Jones, S. Parada, E. Boydens, J.V. Dyck, B. Blanpain, P. Wollants, J. Eur. Ceram. Soc. 26 (2006) 3831–3843.
[8] M.A.L. Braulio, A.G.T. Martinez, A.P. Luz, C. Liebske, V.C. Pandolfelli, Ceram. Int. 37 (2011) 1935–1945.
[9] Y. Kashiwaya, C.E. Cicutti, A.W. Cramb, K. Ishii, ISIJ Int. 38 (1998) 348–356.
[10] S. Sridhar, A.W. Cramb, Metall. Mater. Trans. B 31 (2000) 406–410.
[11] M. Valdez, K. Prapakorn, A.W. Cramb, S. Sridhar, Ironmak. Steelmak. 29 (2002) 47–52.
[12] K.W. Yi, C. Tse, J.H. Park, M. Valdez, A.W. Cramb, S. Sridhar, Scand. J. Metall. 32 (2003) 177–184.
[13] A.B. Fox, M.E. Valdez, J. Gisby, R.C. Atwood, P.D. Lee, S. Sridhar, ISIJ Int. 44 (2004) 836–845.
[14] B.J. Monaghan, L. Chen, J. Non-Cryst. Solids 347 (2004) 254–261.
[15] B.J. Monaghan, L. Chen, J. Sorbe, Ironmak. Steelmak. 32 (2005) 258–264.
[16] B.J. Monaghan, L. Chen, Steel Res. Int. 76 (2005) 348–354.
[17] J.H. Liu, M. Guo, P.T. Jones, F. Verhaeghe, B. Blanpain, P. Wollants J. Am. Ceram. Soc. 90 (2007) 3818–3824.
[18] F. Verhaeghe, J. Liu, M. Guo, S. Arnout, B. Blanpain, P. Wollants, Appl. Phys. Lett. 91 (2007) 124104.
[19] S. Michelic, J. Goriupp, S. Feichtinger, Y.B. Kang, C. Bernhard, J. Schenk, Steel Res. Int. 87 (2016) 57–67.
[20] C. Ren, L. Zhang, J. Zhang, S. Wu, P. Zhu, Y. Ren, Metall. Mater. Trans. B 52 (2021) 3288–3301.
[21] C. Ren, C. Huang, L. Zhang, Y. Ren, Int. J. Miner. Metall. Mater. 30 (2023) 345–353.
[22] J.H. Liu, M. Guo P.T. Jones, F. Verhaeghe, B. Blanpain, P. Wollants, J. Eur. Ceram. Soc. 27 (2007) 1961–1972.
[23] X. Guo, Z.H.I. Sun, J. Van Dyck, M. Guo, B. Blanpain, Ind. Eng. Chem. Res. 53 (2014) 6325–6333.

[24] Z.H.I. Sun, X. Guo, J. Van Dyck, M. Guo, B. Blanpain, AlChE J. 59 (2013) 2907–2916.
[25] T. Tian, Y. Zhang, H. Zhang, K. Zhang, J. Li, H. Wang, Int. J. Appl. Ceram. Technol. 16 (2019) 1078–1087.
[26] Y. Ren, P. Zhu, C. Ren, N. Liu, L. Zhang, Metall. Mater. Trans. B 53 (2022) 682–692.
[27] B.J. Monaghan, L. Chen, Ironmak. Steelmak. 33 (2006) 323–330.
[28] M. Sharma, W. Mu, N. Dogan, JOM 70 (2018) 1220–1224.
[29] M. Sharma, H.A. Dabkowska, N. Dogan, Steel Res. Int. 90 (2019) 1800367.
[30] M. Sharma, N. Dogan, Metall. Mater. Trans. B 51 (2020) 570–580.
[31] B.H. Yoon, K.H. Heo, J.S. Kim, H.S. Sohn, Ironmak. Steelmak. 29 (2002) 214–217.
[32] V.I. Ponomarev, D.M. Kheiker, N.V. Belov, Sovit Physics Crystallogaphy 15 (1970) 1140–1143.
[33] H. Chikama, H. Shibata, T. Emi, M. Suzuki, Mater. Trans. JIM 37 (1996) 620–626.
[34] C.W. Bale, E. Bélisle, P. Chartrand, S.A. Decterov, G. Eriksson, A.E. Gheribi, K. Hack, I.H. Jung, Y.B. Kang, J. Melançon, A.D. Pelton, S. Petersen, C. Robelin, J. Sangster, P. Spencer, M.A. Van Ende, Calphad 55 (2016) 1–19.
[35] C.A. Schneider, W.S. Rasband, K.W. Eliceiri, Nat. Meth. 9 (2012) 671–675.
[36] V.D. Eisenhüttenleute, Slag atlas, 3rd ed., Verlag Stahleisen GmbH, Düsseldorf, Germany, 1995.
[37] C. Xuan, W. Mu, J. Am. Ceram. Soc. 102 (2019) 6480–6497.
[38] R. Li, X. Wang, X. Gao, W. Wang, Y. Zhou, Ceram. Int. 50 (2024) 8249–8259.
[39] B.K.D.P. Rao, D.R. Gaskell, Metall. Trans. B 12 (1981) 773.
[40] A. Habib, J. South. Afr. Stud. 42 (2016) 35–48.
[41] J.H. Park, I.H. Jung, H.G. Lee, ISIJ Int. 46 (2006) 1626–1634.
[42] K.H. Sandhage, G.J. Yurek, J. Am. Ceram. Soc. 71 (1988) 478–489.